Numerical Simulation of Highly Periodical Ge/Si Quantum Dot Array for Intermediate-Band Solar Cell Applications

Yi-Chia Tsai*, Ming-Yi Lee*, Yiming Li*†, and Seiji Samukawa†
*Parallel and Scientific Computing Laboratory, Institute of Communications Engineering,
Department of Electrical and Computer Engineering, National Chiao Tung University,
1001 Ta-Hsueh Rd., Hsinchu 300, Taiwan (e-mail: ymli@faculty.nctu.edu.tw (Y. Li))
†Institute of Fluid Science and WPI-AIMR, Tohoku University, Sendai 980-8577, Japan

***Abstract*—In this work, an efficient method is applied to calculate the miniband structure and density of states for well-ordered Ge/Si quantum dot (QD) array fabricated by combining the self-assemble bio-template and damage-free neutral beam etching. Within the envelop-function framework, this computational model surmounts theoretical approximations of the multi-dimensional Kronig-Penney method and the numerical results provide a guideline for Ge/Si QD solar cell design by simulating the effect of the interdot space and QD's dimension on miniband structure and conversion efficiency.**

I. Introduction

To breakthrough Shockley-Queisser limit [1] which theoretically predicts the maximum efficiency of single-bandgap solar cell, a prospective candidate among the next-generation high efficiency solar cell technologies is the use of quantum dots (QDs) [2]. Because of the quantum confinement, the QDs embedded within the barrier material make a formation of the intermediate band (IB) inside forbidden energy gap of the barrier material. For the intermediate-band solar cell (IBSC), in addition to the absorption of photons by electron transitions between the valence band (VB) and the conduction band (CB), the absorption of sub-bandgap photons through two-photon transition from the VB to the IB and the IB to the CB contributes additional photocurrent so that the efficiency of converting sunlight into energy achieves up to 63% theoretically [3]. When uniform QDs are closely packed as the in-plane superlattice, an unlimited and periodic potential QD layer, the wavefunction of each QD couples with neighboring QDs to broaden the discrete quantum levels to form finite-width miniband. The miniband structure plays a key parameter to determine the two-photon transition and photo-generated carrier transport for QDs solar cell application. In the past, Lazarenkova et al. [4] and Jiang et al. [5] proposed an analytic Kronig-Penney method to describe the three-dimensional (3D) QDs superlattice with assumption of the independent periodic potential for quantum cuboid system. However, with the great development of nano-device processes, a more accurate simulation method without assumption of independent periodic potential and limitation on QDs structure should be developed to instruct realistic QDs fabrication and design.

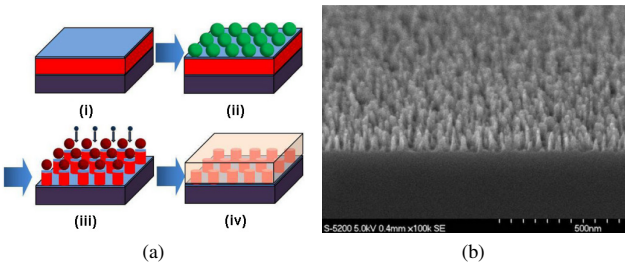

(a) (b)

Fig. 1. An advanced top-down nano-fabrication technology [7]. (a) schematic process flow: (i) Ge/Si stacked layers deposition; (ii) a two-dimensional array ferritin self-assembly and protein shell removal; (iii) damage-free neutral beam etching; (iv) matrix regrowth. (b) SEM image of Ge/Si nanopillars before regrowth matrix for advanced top-down nano-fabrication technology.

In this study, the 3D finite element method (FEM) method reported in our earlier work [6] is further advanced to efficiently simulate the miniband structure and density of states (DoS) for a well-ordered Ge/Si QD array. The QDs array is fabricated by the top-down nanotechnology of integrating neutral beam etching with bio-template [2], [7], which provides great flexibility and accuracy in engineering quantum structures such as independently adjustable diameter, thickness, interdot space, incline angle, matrix materials and so on. The effect of the interdot space, thickness and radius of QDs on band structure and conversion efficiency for solar cell application is investigated.

II. Device Configuration and Model

A. Top-down process

Compared to kinetic-driven bottom-up nanotechnologies, top-down nanotechnologies are more attractive for fabrication of QDs superlattices. However, the traditional top-down process with the lithography process is hardly implanted into quantum size fabrication. The first difficulty is the physical limitation of the conventional photolithographic mask, which is larger than the semiconductor exciton Bohr radius (Si is 4.9 nm). The second difficulty is unavoidably damages induced by the common plasma etching, which act as recombination cen-

978-1-4673-7860-4/15/$31.00 ©2015 IEEE

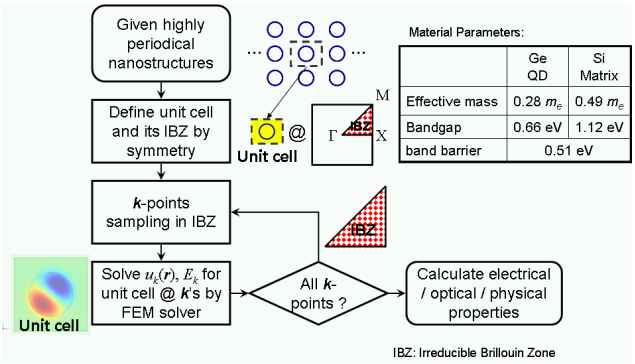

Fig. 2. The simulation flow chart for an in-plane 3D QDs square superlattice and material parameters used for simulation.

ters to degrade optical and electrical properties. By combining the self-assemble bio-template and damage-free neutral beam etching (NBE), a top-down process illustrated in Fig 1a was developed to fabricate sub-10 nm uniform and well aligned type-II Si/Ge QDs superlattice [2], [8]. At first, germanium and silicon are alternately deposited on substrates. The *in situ* measurement is used to precisely control thickness. Next, ferritin molecules self-assemble to form a two-dimensional (2D) array with the spin-coating method. Then high-temperature anealing removes protein shells so that a 2D of metal oxide cores is left as the etching mask. The oxidation surface is isotropically etched by the NF_3 and then is anisotropically etched by Cl_2 neutral beam to form QDs. Finally, matrix silicon is deposited to finish the high-periodical superlattice. The etched Ge/Si nanopillars before regrowth matrix in Fig. 1b exhibits a good uniformity and alignment. This nanofabrication technique can control the QD thickness by the deposition thickness and its diameter by the bio-template, which brings the higher flexibility on engineering quantum levels.

B. The computation model

Within the one-band envelope-function theory, the electronic structure can be described by the Schrödinger equation with the effective mass approximation as

$$\nabla\left[-\frac{\hbar}{2m^*}\nabla\psi(\boldsymbol{r})\right]+V(\boldsymbol{r})\psi(\boldsymbol{r})=E\psi(\boldsymbol{r}), \tag{1}$$

where $\hbar$, m^*, $V(\boldsymbol{r})$, E, $\psi(\boldsymbol{r})$ are the reduced Planck's constant, the effective mass, the position-dependent potential energy, quantum energy levels, and the envelope function respectively. For a periodic superlattice, $V(\boldsymbol{r}+\boldsymbol{R})=V(\boldsymbol{r})$ where $\boldsymbol{R}=n_1\boldsymbol{a}_1+n_2\boldsymbol{a}_2$ is the lattice vector with integers n_1 and n_2. The envelope function will satisfy Bloch theorem that $\psi(\boldsymbol{r})=e^{i\boldsymbol{k}\cdot\boldsymbol{r}}u_k(\boldsymbol{r})$ where $\boldsymbol{k}$ is the lattice wave vector in irreducible Brillouin zone (IBZ). With this bloch wave form, Eq. (1) becomes

$$\nabla\left[-\frac{\hbar}{2m^*}\nabla u_k(\boldsymbol{r})\right]-\frac{i\hbar}{m^*}\boldsymbol{k}\cdot\nabla u_k(\boldsymbol{r}) +\left[V(\boldsymbol{r})+\frac{\hbar k^2}{2m^*}\right]u_k(\boldsymbol{r})=E_{n,k}u_k(\boldsymbol{r}), \tag{2}$$

where n is quantum number, and function $u_k(\boldsymbol{r})$ follows the periodic boundary condition $u_k(\boldsymbol{r}+\boldsymbol{R})=u_k(\boldsymbol{r})$. Fig. 2 shows the simulation flow to solve the bloch function $u_k(\boldsymbol{r})$ and eigenvalue $E_{n,k}$. First, a unit cell formed by two primitive vectors $\boldsymbol{a}_1$ and $\boldsymbol{a}_2$ is defined. Then, based on the symmetry of square superlattice, the $\boldsymbol{k}$-points space is defined in a triangular IBZ. Finally, to get band structure $E_{n,k}$ and bloch function $u_k(\boldsymbol{r})$, Eq. (2) is discretized within a unit cell in real space and solved by a FEM solver for each sampling $\boldsymbol{k}$-point in IBZ. Here the simulation method does not have constrains on geometry and structure of periodic QDs superlattice.

Based on the energy distribution in IBZ, the density of states (DoS) can be calculated numerically using an improved triangle method [9], [10] by dividing the IBZ into a large number of small triangular cells

$$g(E)=\frac{2}{(2\pi)^2}\int_{\mathrm{BZ}}\frac{dl_E}{|\nabla_k E_{n,k}|}=\frac{2}{(2\pi)^2}\sum_{n,l}\frac{l_n(E,\boldsymbol{k}_l)}{|\nabla_k E_n(\boldsymbol{k}_l)|}. \tag{3}$$

The DoS, the number of allowed carrier states per unit area per unit energy, is a key parameter for electronic and optical applications of semiconductor system.

To investigate the effect of band structure on IBSC, the Luque equation [11] is modified to consider the density of QDs and miniband bandwidth for QDs superlattice. With the detailed balance arguments, the current density is given by

$$J=J_{\mathrm{CV}}(\mu_{\mathrm{CV}})+\nu J_{\mathrm{IB}}(\mu_{\mathrm{CI}},\mu_{\mathrm{IV}}), \tag{4}$$

where ν is the volume ratio of QDs to bulk matrix, J_{CV} is photocurrent density induced from the bulk matrix materials [3], J_{IB} is photocurrent density induced from the intermediate bands [11] created by QDs array, and μ_{IJ} is the difference of quasi-Fermi energy between miniband I and miniband J [3], [12]. The current-voltage (J-V) characteristics and the efficiency of the photovoltaic conversion for QDs superlattice are calculated by Eq. (4) together with $V=\mu_{\mathrm{CV}}=\mu_{\mathrm{CI}}+\mu_{\mathrm{IV}}$.

III. Results and Discussion

A. Miniband and Density of States

The top-down process by combining the self-assemble bio-template and damage-free NBE in Fig. 1a is applied to fabricate type-II Ge/Si QDs superlattice [2]. For the IBSC applications, the type-II Ge/Si QDs has advantage of the band-offset mainly lying on the valence band (0.51 eV) that electron can near-freely transport in the conduction band and extra electron/hole pair are pumping out of miniband in band barrier by two-photon transition. This is very near to the ideal IBSC design [3]. By using the simulation flow and adopted parameters in Fig. 2, we calculate the band disperion relation of type II Ge/Si QDs square superlattice as shown in Fig. 3, where QDs is in dimension of the raius 3 nm, thickness 4 nm and interdot space 2.3 nm. There are totally 15 bounded states with energy lower than band barrier 0.51 eV that form 8 separate minibands.

The energy distribution in IBZ for the lowest three bounded bands is shown in Fig. 4a- 4c. The energy for the ground band

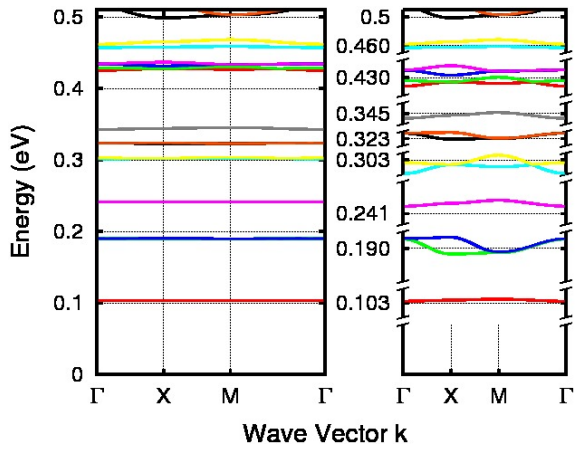

Fig. 3. The band dispersion relation for in-plane 3D Ge/Si QDs superlattice with QD's radius 3 nm, thickness 4 nm and interdot space 2.3 nm. The right figure breaks energy axis into several segments in different scale to highlight the profile of each quantum level. There are totally 15 bounded states with energy lower than band barrier 0.51 eV.

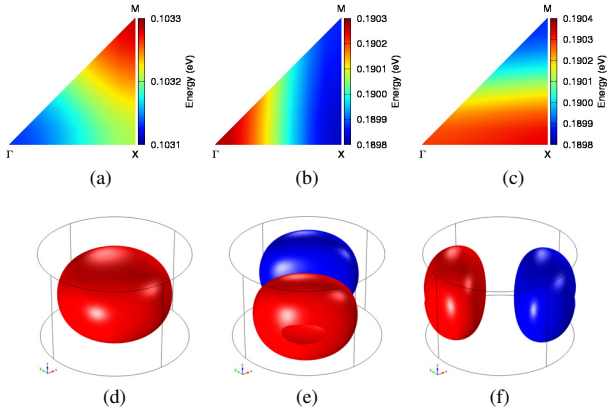

Fig. 4. The energy distribution in IBZ for (a) ground bounded-band $E_{0,k}$ and (b)/(c) first/second excited bounded-band $E_{1,k}/E_{2,k}$. The isosurface of wave function within QD at Γ-point of IBZ for (d) s-orbit E_0 and (e)/(f) degenerate p-orbits E_1 and E_2.

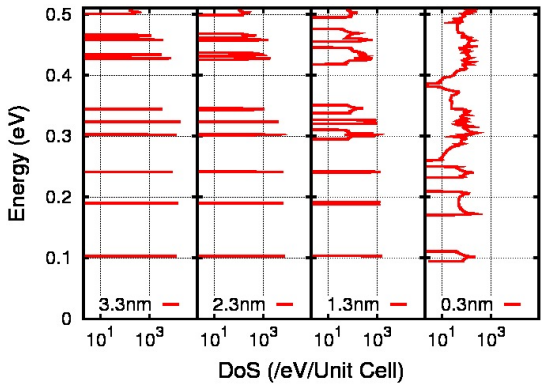

Fig. 5. The density of states for Ge/Si QDs square superlattice with QD radius 3 nm, thickness 4 nm, and varied interdot space from 3.3 nm to 0.3 nm.

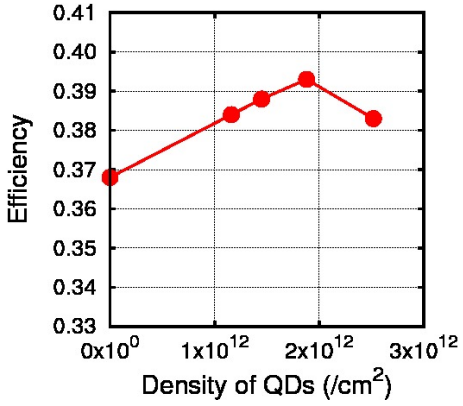

Fig. 6. The conversion efficiency versus QDs density in the range of 10^{12}/cm^2 due to varied interdot space from 3.3 nm to 0.3nm for Ge/Si QDs IBSC under 1000 sun illumination. The data for zero QDs density is calculated from silicon single-bandgap solar cell .

is distributed isotropically in $\boldsymbol{k}$-space and minimum in Γ-point. The energy for the first and second excited bands are constant in k_y and k_x direction respectively. These distributions are close related to their wavefunctions. Fig. 4d- 4f shows the isosurface of wave function within Ge QD at Γ-point ($\boldsymbol{k} = 0$) of IBZ for lowest three bounded-states. The ground state has ellipsoid surface without nodes as the expected s-orbit. The next two states show a two-fold degenerate p-orbit due to symmetry of x-y plane. These energy distributions and wave functions reveal the symmetry of the QDs superlattice.

In addition to the symmetry of the superlattice, the quantum energy levels form the quasi-contineous minibands with finite bandwith due to the QDs coupling with each other. The inter-dot space dtermines the coupling strength. Based on the energy distribution in IBZ in Fig. 4, the DoS is calculated numerically by Eq. (3). Fig. 5 presents the results for QDs superlattice with varied interdot space from 3.3 nm to 0.3 nm. As the interdot space decreasing, QDs interaction between discrete levels increases so that the miniband bandwidth increases and the miniband crossing phenomenon occurs especially for higher excited states. Because the highest excited states are mixed and become continuous energy levels to Si barrier, the effective bandgap of bulk Si decreases with the interdot space. This reduction of effective banbgap impacts much on the conversion efficiency of QDs IBSC in the next discussion.

B. Application on QD Solar Cell

Fig. 6 shows the conversion efficiency for the IBSC consisted of Ge/Si QDs under 1000 sun illumination. The Ge QDs array embedded in bulk silicon contributes additional current by J_{IB} and enlarge the conversion efficiency up to 39.3% with density of QDs as high as 1.88×10^{12}/cm^2 (the interdot space 1.3 nm). However, the conversion efficiency turns around with QDs density 2.52×10^{12}/cm^2 as the interdot space decreases to 0.3 nm. It is a result of smaller open-circuit voltage. The reduced open-circuit voltage in Fig 7 is explained by the reduced effective bandgap, which is a result of higher

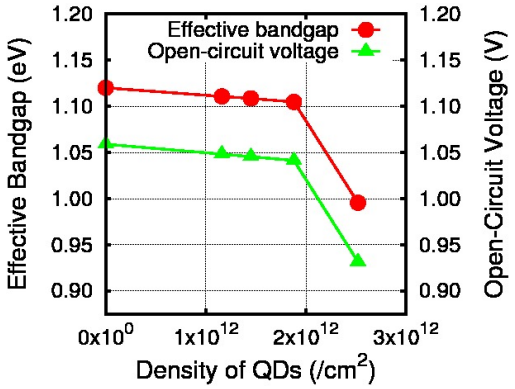

Fig. 7. The effective bandgap voltage and open-circuit voltage versus QDs density in the range of 10^{12}/cm^2 due to varied interdot space from 3.3 nm to 0.3nm for Ge/Si QDs IBSC under 1000 sun illumination. The data for zero QDs density is calculated from silicon single-bandgap solar cell.

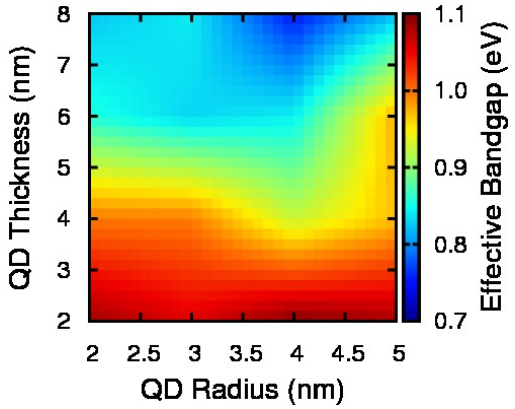

Fig. 8. The effective bandgap variation for varied QD radius and height with interdot space 0.3 nm for Ge/Si QDs IBSC under 1000 sun illumination.

excited states becoming continuous state through miniband crossing under strong QDs interaction between each other as the interdot space decreases. This phenomenon is physically consistent that, as density of Ge QDs is high, Ge QDs array approaches bulk Ge whose bandgap is 0.66 eV and open-circuit voltage is 0.63 V by detailed balance limit for a single bandgap solar cell.

Fig. 8 shows the variation of effective bandgap with varied QDs radius and height when QDs interaction is strong (interdot space 0.3 nm). The reduction of effective bandgap shows more dependence on the QDs thickness. With the QDs thickness going thicker with a fixed radius, the quantum confinement in z-direction becomes weaker that the energy levels of bounded states goes lower and more bounded states locate within silicon barrier. As discussion of miniband crossing phenomenon occurring for higher bounded states, the more bounded states increase the situation of miniband crossing that reduces the effective bandgap. On the other hand, the radius going larger with a fixed thickness also has the weaker quantum confinement on QDs in x-y plane to have more bounded states but weaker interaction between QDs at the same time due to larger distance (sum of radius and interdot) between QDs. Thus these two competing mechanisms induce the non-monotonic dependence of the effective bandgap on the radius.

IV. Conclusion

The FEM method by a unit cell with consideration of translation symmetry was developed to accurately calculate the miniband structure and density of states for a realistic QDs array. For Ge/Si nanodisk array fabricated by an advanced top-down process, the miniband formation and crossing affects sub-bandgap and the effective bandgap of bulk Si, which results in a turn-around phenomenon for conversion efficiency with QDs density. The dependence of effective bandgap on the radius and the thickness of QDs is also studied to provide a guideline for QDs fabrication and design on solar cell application.

Acknowledgment

This work was supported in part by the Ministry of Science and Technology, Taiwan, under Contract No. MOST 103-2221-E-009-180.

References

[1] W. Shockley and H. J. Queisser, "Detailed balance limit of efficiency of p-n junction solar cells," *J. Appl. Phys.*, vol. 32, no. 3, pp. 510–519, 1961.

[2] T. Fujii, T. Okada, M. E. Syazwan, T. Isoda, H. Endo, M. M. Rahman, K. Ito, and S. Samukawa, "Germanium nano disk array fabrication by combination of bio template and neutral beam etching for solar cell application," in *IEEE 40th Photovoltaic Specialist Conference (PVSC)*, 2014, pp. 1033–1036.

[3] A. Luque and A. Martí, "Increasing the efficiency of ideal solar cells by photon induced transitions at intermediate levels," *Phys. Rev. Lett.*, vol. 78, pp. 5014–5017, 1997.

[4] O. L. Lazarenkova and A. A. Balandin, "Miniband formation in a quantum dot crystal," *J. Appl. Phys.*, vol. 89, no. 10, pp. 5509–5515, 2001.

[5] C.-W. Jiang and M. A. Green, "Silicon quantum dot superlattices: Modeling of energy bands, densities of states, and mobilities for silicon tandem solar cell applications," *J. Appl. Phys.*, vol. 99, p. 114902, 2006.

[6] W. Hu, M. F. Budiman, M. Igarashi, M.-Y. Lee, Y. Li, and S. Samukawa, "Modeling miniband for realistic silicon nanocrystal array," *Math. Comput. Model.*, vol. 58, pp. 306–311, 2013.

[7] M. Igarashi, M. F. Budiman, W. Pan, W. Hu, N. Usami, and S. Samukawa, "Quantum dot solar cells using 2-dimensional array of 6.4-nm-diameter silicon nanodisks fabricated using bio-templates and neutral beam etching," *Appl. Phys. Lett.*, vol. 101, p. 063121, 2012.

[8] W. Hu, M. M. Rahman, M.-Y. Lee, Y. Li, and S. Samukawa, "Simulation study of type-II Ge/Si quantum dot for solar cell applications," *J. Appl. Phys.*, vol. 114, p. 124509, 2013.

[9] J.-H. Lee, T. Shishidou, and A. J. Freeman, "Improved triangle method for two-dimensional Brillouin zone integrations to determine physical properties," *Phys. Rev. B*, vol. 66, p. 233102, 2002.

[10] P. E. Blöchl, O. Jepsen, and O. K. Andersen, "Improved tetrahedron method for Brillouin-zone integrations," *Phys. Rev. B*, vol. 49, pp. 16 223–16 233, 1994.

[11] L. Cuadra, A. Martí, and A. Luque, "Influence of the overlap between the absorption coefficients on the efficiency of the intermediate band solar cell," *IEEE Trans. Electron Devices*, vol. 51, pp. 1002–1007, 2004.

[12] K. Schick, E. Daub, S. Finkbeiner, and P. Würfel, "Verification of a generalized planck law for luminescence radiation from silicon solar cells," *Appl. Phys. A.*, vol. 54, pp. 109–114, 1992.